



Article

Multiscale Modelling and Mechanical Anisotropy of Periodic Cellular Solids with Rigid-Jointed Truss-Like Microscopic Architecture

Victor E. L. Gasparetto and Mostafa S. A. ElSayed *

Department of Mechanical and Aerospace Engineering, Carleton University, Ottawa, ON K1S 5B6, Canada; victorgasparetto@cmail.carleton.ca

* Correspondence: mostafa.elsayed@carleton.ca; Tel.: +1-613-520-2600 (ext. 4138)

Abstract: This paper investigates the macroscopic anisotropic behavior of periodic cellular solids with rigid-jointed microscopic truss-like architecture. A theoretical matrix-based procedure is presented to calculate the homogenized stiffness and strength properties of the material which is validated experimentally. The procedure consists of four main steps, namely, (i) using classical structural analysis to determine the stiffness properties of a lattice unit cell, (ii) employing the Bloch's theorem to generate the irreducible representation of the infinite lattice, (iii) resorting to the Cauchy–Born Hypothesis to express the microscopic nodal forces and deformations in terms of a homogeneous macroscopic strain field applied to the lattice, and (iv) employing the Hill–Mandel homogenization principle to obtain the macro-stiffness properties of the lattice topologies. The presented model is used to investigate the anisotropic mechanical behavior of 13 2D periodic cellular solids. The results are documented in three set of charts that show (i) the change of the Young and Shear moduli of the material with respect to their relative density; (ii) the contribution of the bending stiffness of microscopic cell elements to the homogenized macroscopic stiffness of the material; and (iii) polar diagrams of the change of the elastic moduli of the cellular solid in response to direction of macroscopic loading. The three set of charts can be used for design purposes in assemblies involving the honeycomb structures as it may help in selecting the best lattice topology for a given functional stiffness and strength requirement. The theoretical model was experimentally validated by means of tensile tests performed in additively manufactured Lattice Material (LM) specimens, achieving good agreement between the results. It was observed that the model of rigid-jointed LM (RJLM) predicts the homogenized mechanical properties of the LM with higher accuracy compared to those predicted by pin-jointed models.



Citation: Gasparetto, V.E.L.; ElSayed, M.S.A. Multiscale Modelling and Mechanical Anisotropy of Periodic Cellular Solids with Rigid-Jointed Truss-Like Microscopic Architecture. *Appl. Mech.* **2021**, *2*, 331–355. <https://doi.org/10.3390/applmech2020020>

Received: 20 April 2021
Accepted: 27 May 2021
Published: 1 June 2021

Publisher's Note: MDPI stays neutral with regard to jurisdictional claims in published maps and institutional affiliations.



Copyright: © 2021 by the authors. Licensee MDPI, Basel, Switzerland. This article is an open access article distributed under the terms and conditions of the Creative Commons Attribution (CC BY) license (<https://creativecommons.org/licenses/by/4.0/>).

Keywords: lattice materials; rigid-jointed micro-truss; cellular solids; honeycombs; anisotropy

1. Introduction

A periodic cellular solid, also known as a LM, is a periodic micro-architected structure designed by tessellating a unit cell in an infinite periodicity. The unit cell is considered as the material's Representative Volume Element (RVE), sufficient to predict its macroscopic characteristics [1–3]. To be considered a periodic structure, the unit cell must present a degree of symmetry, which is given by the Bravais lattice symmetry [4]. This category of structure is known for its unusual mechanical properties not found in natural bulk solids, which makes them suitable for applications in a plethora of engineering areas, such as mechanical [5–7], aerospace [8–10] or biomedical [11–13]. Some relevant characteristics explored in recent works are related to auxetic behavior [14–16], elevated mechanical strength and stiffness [17–19], exceptional elastodynamic behavior [20–24].

LMs are classified into two categories, bending and stretching dominated [25–27], when considering the small deformations hypothesis. A stretching dominated lattice structure, does not present internal mechanisms, when performing a determinacy analysis,

therefore its elements are mainly loaded in tension or compression [28]. Modeling a stretching dominated structure as pin-jointed is sufficient to predict its homogenized macroscopic mechanical characteristics [29]. Even when its joints are considered as rigid, the arising bending moments are often neglected. By relaxing the constraint of small deformations, some special cases arise. For instance, a Triangular-Triangular lattice topology which is classified as stretching-dominated, will be bending-dominated under the load of pure dilation as this lattice tends to transform to the configuration of Kagome lattice [30]. Bending dominated structures, on the other hand, contain internal active mechanisms that are not developed by states of self-stress [31], hence being suppressed due to nodal rotational stiffness within the lattice connectivity.

Several numeric and analytic methods have been proposed to effectively model properties of RJLM [32] in which the response of a single unit cell or a finite number of them are investigated. Other analytical methods modelled the LM as a continuum. Those models provide inaccurate results when the in-plane bending of the cell elements of a RJLM is taken into consideration [33]. To overcome this issue, a micro-polar continuum model has been used for the characterization of LMs [34,35]. More recently, the use of the *Bloch's* theorem [36], commonly applied in solid state Physics, has been proposed to model the propagation of the static and the kinematic wave-functions in an infinite lattice structure [37–40]. An interesting research by Niu and Wang [41] presented the concurrent determination of specific elastic properties of RJLM periodic Kagome honeycomb lattice with its wave propagation directionality, where it was possible to characterize an optimum configuration of the structure in order to achieve maximization of its stiffness and strength.

A novel matrix-based methodology is proposed in this paper to model the effective stiffness properties of a RJLM. The classical matrix methods of structural analysis [38,42] are used to derive the stiffness of the finite structure of the lattice unit cell. The *Bloch's* theorem is employed to reduce the stiffness system to the irreducible representation of the infinite lattice structure. The *Cauchy-Born* Hypothesis [43–46], in turn, is used to determine the micro-nodal forces and deformations defined by a homogeneous macro-strain field applied to the lattice. Through the principle of virtual work [47] and *Hill-Mandel* [45] of macro-homogenization, we derive the macro-stiffness properties of a RJLM. The method is employed to formulate closed-form expressions of in plane stiffness of 13 2D lattice topologies. In addition, the *Bond-stress* and strain orthogonal transformations [48,49] are used to study the anisotropic behavior of the homogenized macroscopic stiffness of LMs with selected cell topologies. Moreover, we experimentally validated the numerical method implemented with tensile and shear test in a specimen designed following the criteria presented in the paper, achieving low error in the prediction of the elastic moduli and strength of the lattice materials. The framework created allows the designer to effectively estimate the mechanical properties of any desired 2D periodic lattice unit-cell topology. Finally, we also presented design charts for the 13 lattice topologies investigated, which allows one to effectively estimate the elastic properties of the lattice unit-cells for a given relative density, which can be calculated from the geometrical parameters of the unit-cell designed. The design charts are also generated as polar coordinate maps, where it is possible to capture the effect of anisotropic behavior of the lattice topologies, therefore indicating the best orientation a LM can be loaded to resist a macroscopic loading applied in a given direction.

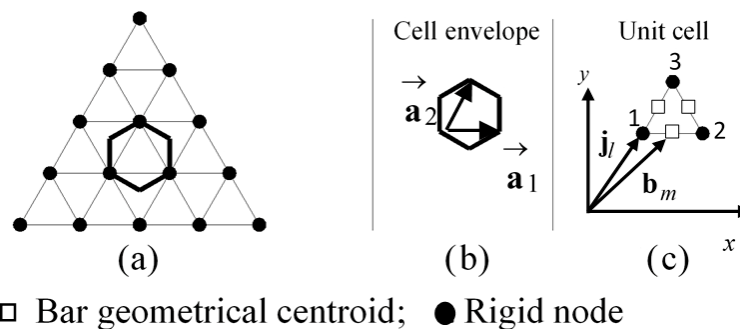
The paper is divided in six sections. Succeeding this introduction, the modeling procedure to characterize the stiffness properties of RJLMs is presented. In the third section, the modeling procedure is used to determine the stiffness properties of 13 different topologies of 2D LMs. Accuracy of the theoretical modeling procedure is verified experimentally in Section 4. In the fifth section, the anisotropic response of the lattices is investigated and charts that show the change of the elastic moduli with respect to macroscopic loading direction are presented. In section six, the results are discussed along with the paper conclusions.

2. Methodology

A LM is constructed by infinitely tessellating a unit cell. A similar construction is commonly applied in solid state physics to describe the arrangement of atomic crystals in a solid [4]. An atomic crystal is assumed as a mathematical superposition of two identities, namely, the lattice and the bases. The lattice is defined as an infinitely periodic positioning of nodes in space [50,51], where bases are the mathematical description of the pattern in every cell translation.

Likewise, the above description can be adopted in continuum mechanics to model a LM. The unit cell is the minimum division of the lattice and is defined as the superposition of two identities, namely, the cell envelope and the bases. The former describing the periodic structure is expressed with the primitive bases, \vec{a}_k , of the lattice translational symmetry, where $k \in \{1, \dots, n\}$ and $n = 2$ or $n = 3$ in 2D or 3D, respectively. The latter represents the physical network defined by two groups, the nodal and the bar bases group.

Figure 1 depicts the described concept, with respect to the 2D triangular lattice. Figure 1a shows the microstructure of the LM. The envelope of a possible unit cell is shown with the bold lines in Figure 1a,b. The latter also illustrates the primitive bases \vec{a}_1 and \vec{a}_2 . Figure 1c, on the other hand, depicts the bar arrangement vectors, b_m , and node arrangement vectors, j_l , of the physical structure of the unit cell, where $m \in \{1, 2, \dots, b\}$ and $l \in \{1, 2, \dots, j\}$. b and j are, respectively, the number of bars and nodes within the unit cell.



□ Bar geometrical centroid; ● Rigid node

Figure 1. Triangular lattice. (a) Tessellated lattice, (b) Cell envelope, (c) Unit cell.

2.1. Constitutive Stiffness of the RJLM Unit Cell

The stiffness systems of a structure that contains b elements linked by j nodes can be written as the following:

$$Kd = f \tag{1}$$

where $K \in R^{nj \times nj}$ is the constitutive stiffness matrix of the structure that associates its nodal deformation vector, $d \in R^{nj}$, to the applied force vector, $f \in R^{nj}$ [42]. On the other hand, the stiffness system of a frame element, k , can be expressed as:

$$K_k^l d_k^l = \{K_{k_l}^{bar} + K_{k_l}^{beam}\} d_k^l = f_k^l \tag{2}$$

$$K_{k_l}^{bar} = \frac{EA}{l_k} \begin{bmatrix} 1 & 0 & 0 & -1 & 0 & 0 \\ 0 & 0 & 0 & 0 & 0 & 0 \\ 0 & 0 & 0 & 0 & 0 & 0 \\ -1 & 0 & 0 & 1 & 0 & 0 \\ 0 & 0 & 0 & 0 & 0 & 0 \\ 0 & 0 & 0 & 0 & 0 & 0 \end{bmatrix}, K_{k_l}^{beam} = \frac{EI}{l_k^3} \begin{bmatrix} 0 & 0 & 0 & 0 & 0 & 0 \\ 0 & 12 & 6l_k & 0 & -12 & 6l_k \\ 0 & 6l_k & 4l_k^2 & 0 & -6l_k & 2l_k^2 \\ 0 & 0 & 0 & 0 & 0 & 0 \\ 0 & -12 & -6l_k & 0 & 12 & -6l_k \\ 0 & 6l_k & 2l_k^2 & 0 & -6l_k & 4l_k^2 \end{bmatrix} \tag{3}$$

where $\mathbf{K}_{k_l}^{bar}$ and $\mathbf{K}_{k_l}^{beam}$ are the local element axial and bending constitutive stiffness matrices, respectively, as $\mathbf{K}_k^l = \mathbf{K}_{k_l}^{bar} + \mathbf{K}_{k_l}^{beam}$ is the frame element total stiffness matrix. E, A, I and l_k are, respectively, the Young's modulus of the solid material, the cross-sectional area, the second moment of area and the length of the bar element. f_k^l and d_k^l are, respectively, the nodal force and the nodal displacement vectors of element k in the element local coordinate system $(x_1 - y_1)$. It should be noted that $E, A,$ and I are assumed as common for all elements of the unit cell while the element length is varied.

A formulation similar to Equations (2) and (3) can be obtained for each element in the unit cell, and the assembled global stiffness system of the unit cell finite structure is given as:

$$\mathbf{K}d = \{ \mathbf{K}^{bar} + \mathbf{K}^{beam} \} d = f \tag{4}$$

2.2. Stiffness System of a RJLM

The Bloch's theorem [36] is employed to generate the irreducible form of the stiffness system of the unit cell. This constitutes the stiffness of the unbounded lattice. Similar to the approach found in [27,37], the Bloch's theorem is used here to describe the propagation of the wave-function over a LM.

2.2.1. Bloch's Theorem

A wave-function, $w(p_l, \omega) \in C^2$, propagating over an infinite lattice can be written as:

$$w(p_l, \omega) = w(j_l + \vec{R}, \omega) = w(j_l, \omega)e^{2\pi i \omega \vec{R}}, \quad \forall l \in \{1, 2, \dots, J\} \tag{5}$$

$$w(q_m, \omega) = w(b_m + \vec{R}, \omega) = w(b_m, \omega)e^{2\pi i \omega \vec{R}}, \quad \forall l \in \{1, 2, \dots, B\} \tag{6}$$

where $p_l = j_l + \vec{R}$ and $q_m = b_m + \vec{R}$ are, respectively, the position vectors of node l and bar m of the LM and \vec{R} is the direct translational vector of any unit cell of the LM. $\omega = (\omega_1, \omega_2)$, ω_1 and ω_2 being the covariant components of ω , are found from the irreducible Brillouin zone of the reciprocal lattice space. J and B are, respectively, the independent nodes and bars within the unit cell envelope. $i = \sqrt{-1}$ is the complex number and C is the set of all complex numbers. The following section presents the transformation matrices that is applied to reduce the wave-functions and constitutive matrices. The procedure imposes periodic boundary conditions to the unit cell [52,53].

2.2.2. Transformation Matrices

The kinematic transformation matrix is obtained as the following. Consider the generic unit cell depicted in Figure 2; when applying the Bloch's theorem the relations below can be written:

$$\begin{aligned} q_R &= e^{\mu_x} q_L, \quad q_T = e^{\mu_y} q_B, \quad q_{RB} = e^{\mu_x} q_{LB}, \\ q_{LT} &= e^{\mu_y} q_{LB}, \quad q_{RT} = e^{\mu_x + \mu_y} q_{LB} \end{aligned} \tag{7}$$

where q is the deformation function of a generic node; T, B, L and R denote top, bottom, left and right, respectively; μ_x and μ_y are expressed as:

$$\mu_x = 2\pi\omega_1 i, \quad \mu_y = 2\pi\omega_2 i \tag{8}$$

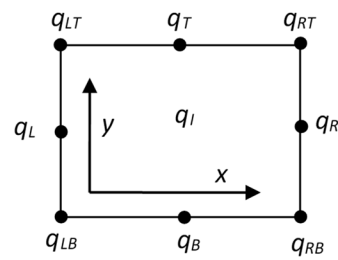


Figure 2. Generic unit cell with its periodic kinematic boundaries.

Equation (7) can be written in matrix terms as:

$$q = T\tilde{q} \tag{9}$$

$$T = \begin{bmatrix} \mathbf{I} & 0 & 0 & 0 \\ 0 & \mathbf{I} & 0 & 0 \\ 0 & \mathbf{I}e^{\mu_y} & 0 & 0 \\ 0 & 0 & \mathbf{I} & 0 \\ 0 & 0 & \mathbf{I}e^{\mu_x} & 0 \\ 0 & 0 & 0 & \mathbf{I} \\ 0 & 0 & 0 & \mathbf{I}e^{\mu_y} \\ 0 & 0 & 0 & \mathbf{I}e^{\mu_x+\mu_y} \end{bmatrix}, q = \begin{bmatrix} q_I \\ q_B \\ q_T \\ q_L \\ q_R \\ q_{LB} \\ q_{RB} \\ q_{LT} \\ q_{RT} \end{bmatrix}, \tilde{q} = \begin{bmatrix} q_I \\ q_B \\ q_L \\ q_{LB} \end{bmatrix} \tag{10}$$

where T is the transformation matrix to the reduced degrees of freedom of the infinite LM structure, and \mathbf{I} is an identity matrix of same size as the unit cell nodal degrees of freedom. The reduced wave-functions of the nodal displacements, by application of the transformation matrix, is given as:

$$d = T\tilde{d} \tag{11}$$

where \tilde{d} is the reduced nodal displacement vector. The same concept, used for the kinematic transformation matrix, can be applied to generate the equilibrium transformation matrix. For the cluster of four generic unit cells shown in Figure 3, the application of the Bloch's theorem allows writing the equations below:

$$\begin{aligned} f_R + e^{\mu_x} f_L = 0, & \quad f_T + e^{\mu_y} f_B = 0, \\ f_{RT} + e^{\mu_x} f_{LT} + e^{\mu_y} f_{RB} + e^{\mu_x+\mu_y} f_{LB} = 0 \end{aligned} \tag{12}$$

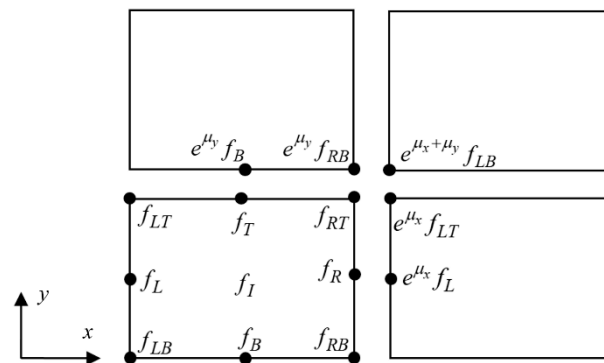


Figure 3. Unit cell with its periodic equilibrium boundaries.

Equation (12) can be arranged as:

$$\tilde{f} = T^H f = 0 \tag{13}$$

where $\tilde{f} = [f_I \ f_B \ f_L \ f_{LB}]^T, f = [f_I \ f_B \ f_T \ f_L \ f_R \ f_{LB} \ f_{RB} \ f_{LT} \ f_{RT}]^T$ and T^H is the Hermitian (the conjugate transpose) of the transformation matrix T .

Equations (11) and (13) are substituted in the constitutive global stiffness system of the unit cell to derive its periodic reduced form as:

$$\tilde{K}\tilde{d} = \tilde{f} \tag{14}$$

where \tilde{K} is the reduced stiffness matrix of the LM, expressed as:

$$\tilde{K} = T^H K T \tag{15}$$

2.3. Effective Macro-Stiffness of a RJLM

The stiffness properties of the microstructure of the LM are homogenized to establish its macro-stiffness properties. This procedure can be performed by means of the employment of the *Cauchy-Born* hypothesis [43–46], as described below.

2.3.1. Cauchy-Born Hypothesis

The definition of the *Cauchy-Born* hypothesis [43] states that the infinitesimal displacement field of a periodic node in a LM structure is given by:

$$d(j_l + \vec{R}, \bar{\epsilon}) = d(j_l, \bar{\epsilon} = 0) + \bar{\epsilon} \cdot \vec{R} \tag{16}$$

where $d(j_l, \bar{\epsilon} = 0)$ is the l nodal displacement vector. Assuming that the nodes described by the position vectors j_l and $j_l + \vec{R}$, are the two rigid nodes i and j within a LM structure, then Equation (16) can be written as:

$$\begin{bmatrix} d_{ix} \\ d_{iy} \\ \theta_i \end{bmatrix} = \begin{bmatrix} d_{jx} \\ d_{jy} \\ \theta_j \end{bmatrix} + \begin{bmatrix} \epsilon_{xx} & \epsilon_{xy} \\ \epsilon_{yx} & \epsilon_{yy} \\ 0 & 0 \end{bmatrix} \begin{bmatrix} x_i - x_j \\ y_i - y_j \end{bmatrix}, \text{ in 2D} \tag{17}$$

where d_{ix} and d_{iy} are, respectively, the vectorial displacement components of the node in the x and y directions and node i is the dependent node, while node j is the independent node. The parameter θ_i represents the rotation of the node in the xy -plane. By using the concept of engineering strain [54], Equation (17) is modified to:

$$\begin{bmatrix} d_{ix} \\ d_{iy} \\ \theta_i \end{bmatrix} = \begin{bmatrix} d_{jx} \\ d_{jy} \\ \theta_j \end{bmatrix} + \begin{bmatrix} \epsilon_{xx} & \frac{1}{2}\epsilon_{xy} \\ \frac{1}{2}\epsilon_{yx} & \epsilon_{yy} \\ 0 & 0 \end{bmatrix} \begin{bmatrix} x_i - x_j \\ y_i - y_j \end{bmatrix}, \text{ in 2D} \tag{18}$$

which is given by:

$$\begin{bmatrix} d_{ix} \\ d_{iy} \\ \theta_i \end{bmatrix} = \begin{bmatrix} d_{jx} \\ d_{jy} \\ \theta_j \end{bmatrix} + \begin{bmatrix} (x_i - x_j) & 0 & \frac{1}{2}(y_i - y_j) \\ 0 & (y_i - y_j) & \frac{1}{2}(x_i - x_j) \\ 0 & 0 & 0 \end{bmatrix} \begin{bmatrix} \epsilon_{xx} \\ \epsilon_{yy} \\ \epsilon_{xy} \end{bmatrix} \text{ or } \mathbf{d}_i = \mathbf{d}_j + E\bar{\epsilon} \tag{19}$$

Applying this boundary condition to the nodal displacement vector, \mathbf{d} , of the unit cell returns:

$$\mathbf{d} = T\tilde{\mathbf{d}} + E\bar{\epsilon} \tag{20}$$

Equation (20) is the rigid-jointed modified kinematic boundary condition of the *Cauchy-Born* Hypothesis. Substituting Equation (17) into the constitutive stiffness system of the unit cell (Equation (4)) yields:

$$K\{T\tilde{\mathbf{d}} + E\bar{\epsilon}\} = \{K^{bar} + K^{beam}\}\{T\tilde{\mathbf{d}} + E\bar{\epsilon}\} = \mathbf{f} \tag{21}$$

Pre-multiplying Equation (21) by the Hermitian of the transformation matrix, T^H , and substituting Equation (13) into the outcome, results in:

$$T^H K \{ T \tilde{d} + E \bar{\epsilon} \} = T^H \{ K^{bar} + K^{beam} \} \{ T \tilde{d} + E \bar{\epsilon} \} = T^H f = \tilde{f} = 0 \tag{22}$$

Rearranging Equation (22), results in:

$$T^H \{ K^{bar} + K^{beam} \} T \tilde{d} = -T^H \{ K^{bar} + K^{beam} \} E \bar{\epsilon} \tag{23}$$

Equation (23) is divided into two matrix systems that are given by:

$$\tilde{K}^{bar} \tilde{d} = -T^H K^{bar} E \bar{\epsilon} \tag{24}$$

$$\tilde{K}^{beam} \tilde{d} = -T^H K^{beam} E \bar{\epsilon} \tag{25}$$

where $\tilde{K}^{bar} = T^H K^{bar} T$ and $\tilde{K}^{beam} = T^H K^{beam} T$ are respectively the axial (bar) and bending (beam) stiffness matrices.

2.3.2. Microscopic Nodal Deformations in Terms of Macro-Strain Field

The microscopic nodal deformation should be computed in terms of macro-strain field using Equations (24) and (25). This can be done by multiplying both sides of Equations (24) and (25) with the inverted stiffness matrices. To invert the stiffness matrices, all non-pivotal modes in their column and row spaces have to be eliminated. The non-pivotal modes are related to the rigid-body motion, since the LM is not constrained, and the modes associated with microscopic internal mechanisms within the lattice. The non-pivotal modes can be determined by computing the reduced row echelon form [55] of the two matrices \tilde{K}^{bar} and \tilde{K}^{beam} . The resulting non-singular stiffness matrices can be inverted and an expression of the microscopic nodal displacements, related to the given macroscopic strain field, can be expressed as:

$$\tilde{d}_{bar} = - \left(\tilde{K}_{red}^{bar} \right)^{-1} \left(T^H K^{bar} E \right)_{red} \bar{\epsilon} \tag{26}$$

$$\tilde{d}_{beam} = - \left(\tilde{K}_{red}^{beam} \right)^{-1} \left(T^H K^{beam} E \right)_{red} \bar{\epsilon} \tag{27}$$

where \tilde{d}_{bar} and \tilde{d}_{beam} are, respectively, the microscopic nodal deformations corresponding to the axial and the bending behavior of the LM. \tilde{K}_{red}^{bar} and \tilde{K}_{red}^{beam} are, respectively, the bar and the beam non-singular, reduced, stiffness matrices generated after eliminating modes associated with the rigid-body modes and the internal network mechanisms.

The deformation of the unit cell nodes is found by substituting Equations (26) and (27) into Equation (20), which results in:

$$d_{bar} = T \tilde{d}_{bar} + E \bar{\epsilon} = \left\{ -T \left(\tilde{K}_{red}^{bar} \right)^{-1} \left(T^H K^{bar} E \right)_{red} + E \right\} \bar{\epsilon} \tag{28}$$

$$d_{beam} = T \tilde{d}_{beam} + E \bar{\epsilon} = \left\{ -T \left(\tilde{K}_{red}^{beam} \right)^{-1} \left(T^H K^{beam} E \right)_{red} + E \right\} \bar{\epsilon} \tag{29}$$

The equations of the generalized microscopic nodal forces, with respect to the macroscopic strain field, can be computed by direct substitution of Equations (28) and (29) into Equation (4) as:

$$f_{bar} = K^{bar} d_{bar} = K^{bar} \left\{ -T \left(\tilde{K}_{red}^{bar} \right)^{-1} \left(T^H K^{bar} E \right)_{red} + E \right\} \bar{\epsilon} \tag{30}$$

$$f_{beam} = K^{bar} d_{beam} = K^{bar} \left\{ -T(\tilde{K}_{red}^{beam})^{-1} (T^H K^{beam} E)_{red} + E \right\} \bar{\epsilon} \tag{31}$$

2.3.3. Homogenized Macro-Stiffness of LMs

The generalized nodal forces and deformations, formulated in the previous section, are used to derive the macro-stiffness properties of the RJLMs by applying the principle of virtual work [47] and the Hill-Mandel macro-homogeneity principle [45], as:

$$K_L^{bar} = \left(\frac{EA}{2|A|} \right) \left((M_{bar}^f)^T (M_{bar}^d) \right) \tag{32}$$

$$K_L^{beam} = \left(\frac{EI}{2|A|} \right) \left((M_{beam}^f)^T (M_{beam}^d) \right) \tag{33}$$

where $|A|$ is the planar area of the unit cell. K_L^{bar} and K_L^{beam} are, respectively, the homogenized, fourth order, axial and bending stiffness tensors of the LM. M_{bar}^f and M_{beam}^f are respectively the compatibility matrices of macroscopic strain field and microscopic force vector that is applied to the unit-cell nodes, considering the axial and bending stiffness contribution. Similarly, M_{bar}^d and M_{beam}^d are respectively the compatibility matrices between the macroscopic strain field and the microscopic nodal displacements in the lattice unit-cell structure, considering the axial and bending components of the stiffness matrix. The relative density, $\bar{\rho}_L$, of a 2D LM is given by:

$$\bar{\rho}_L = \frac{\rho_L}{\rho} = C_\rho \left(\frac{H}{L} \right) \tag{34}$$

where C_ρ is a constant parameter that depends on the geometry of the unit cell and H is the in-plane thickness of the microscopic element of the 2D lattice; $\bar{\rho}_L$, ρ_L and ρ are respectively, the relative density of the LM, the LM density and the density of the solid material. If we consider an out-of-plane depth of the 2D lattice equal to a unit length, $L = 1$, and substitute Equation (34) into Equations (32) and (33) we obtain:

$$K_L^{bar} = \left(\frac{E}{2|A|} \right) \left(\frac{\bar{\rho}_L}{C_\rho} \right) \left((M_{bar}^f)^T M_{bar}^d \right) \tag{35}$$

$$K_L^{beam} = \left(\frac{E}{2|A|} \right) \left(\frac{\bar{\rho}_L}{C_\rho} \right)^3 \left((M_{beam}^f)^T M_{beam}^d \right) \tag{36}$$

With the macroscopic stiffness matrix determined, the macro-compliance matrix can be found by calculating the inverse of the stiffness matrix, where $C_L = K_L^{-1}$ is the linearly elastic fourth order compliance tensor of the LM, that can be further used to calculate the LM elastic moduli, which is described by:

$$C_L = (K_L^{bar} + K_L^{beam})^{-1} = \begin{bmatrix} C_{xxxx} & C_{xxyy} & C_{xxxy} \\ C_{yyxx} & C_{yyyy} & C_{yyxy} \\ C_{xyxx} & C_{xyyy} & C_{xyxy} \end{bmatrix} \tag{37}$$

It is possible, then, to write a relation between the macroscopic strain field, $\bar{\epsilon} = [\epsilon_{xx} \ \epsilon_{yy} \ \epsilon_{xy}]^T$, and the stress field, $\bar{\sigma} = [\sigma_{xx} \ \sigma_{yy} \ \sigma_{xy}]^T$, as in the elastic stress Hooke's law equation:

$$\bar{\epsilon} = C_L \bar{\sigma} \tag{38}$$

The elastic moduli and Poisson coefficient can finally be determined by:

$$(E_L)_{xx} = \frac{1}{C_{xxxx}}, \quad (E_L)_{yy} = \frac{1}{C_{yyyy}}, \quad (G_L)_{xy} = \frac{1}{C_{xyxy}} \tag{39}$$

$$(v_L)_{yx} = \frac{-C_{xxyy}}{C_{xxxx}}, (v_L)_{xy} = \frac{-C_{yyxx}}{C_{yyyy}} \tag{40}$$

where $(E_L)_{xx}$, $(E_L)_{yy}$, $(G_L)_{xy}$ are the homogenized Young moduli and shear modulus, respectively, for each principal direction in the cartesian plane. $(v_L)_{yx}$ and $(v_L)_{xy}$ are the directional Poisson coefficients of the lattice material.

2.4. Strength Properties of a RJLM

From the previously determined equations, it is possible to extend them to estimate the RJLM strength. To do so, it is necessary to define the microscopic cell deformation vector, d , with respect to the macroscopic strain field, $\bar{\epsilon}$. This is possible by means of the application of the compatibility matrix previously introduced, M_{bar}^d and M_{beam}^d . They are related as in the following equation:

$$d = d_{bar} + d_{beam} = (M_{bar}^d + M_{beam}^d) \bar{\epsilon} = M_G \bar{\epsilon} \tag{41}$$

where d_{bar} and d_{beam} are the cell element deformations, and M_G is defined as the global compatibility matrix. An in-depth explanation about the calculation of the compatibility matrix can be found in the work of ElSayed and Pasini [27]. The element strain can be computed by pre-multiplying Equation (49) by the reciprocal element length matrix, M_L , establishing the relationship between the microscopic cell element strain, ϵ_μ , and the macroscopic strain field, as in the following relation:

$$\epsilon_\mu = M_L d = M_L M_G \bar{\epsilon} \tag{42}$$

The macroscopic strain is translated into microscopic strain with significant portion being imparted by microscopic bending stiffness in bending dominated lattices and mainly imparted by tensional stiffness in stretching dominated lattices. Using Equation (38) in Equation (42) and multiplying by the material Young modulus, E , one obtains:

$$\sigma_\mu = \Gamma \bar{\sigma}, \Gamma = E M_L M_G C_L \tag{43}$$

where σ_μ is the microscopic cell element stress, and Γ is a matrix dependent on the unit cell topology analyzed and on the microscopic cell element deformations. Equation (43) is used to evaluate the strength properties of the lattice topologies by means of the application of three macroscopic stress fields, $\bar{\sigma}$, considering a single direction in each case. The least resistant element in the lattice unit cell, when subjected to the stress field, will represent the critical macroscopic strength of the lattice material. The relation is given by the following equation:

$$\sigma_L^{cr} = \frac{\sigma_\mu^{cr}}{\max(\Gamma(:, i))} = C_\sigma(i) \sigma_\mu^{cr} \tag{44}$$

where $C_\sigma(i)$ is a coupling coefficient between the macroscopic and microscopic strength of the lattice material, for the x -, y - and xy - directions. This criterion to assess the macroscopic strength of the lattice material conservatively considers that the entire lattice fails when one microscopic element of a unit cell fails. The parameter σ_μ^{cr} refers to the solid material property of comparison for failure analysis. In this paper, the solid material plastic yield strength is considered to evaluate the tensile strength of the lattice. Therefore, the critical microscopic element stress is set equal to the material yield strength, i.e., $\sigma_\mu^{cr} = \sigma_{ys}$. For an isotropic and ductile material, the plastic shear strength can be easily determined by the relation $\tau_{ys} = \sigma_{ys}/2$, which is obtained from the Mohr's circle in pure shear loading, and thus is used to estimate the critical shear strength of the lattice material.

3. Stiffness Property Charts

The methodology described in Section 2 is applied here to compute the relative stiffness of 13 RJLM topologies. The lattice topologies and their respective unit cells with

the direct lattice bases are depicted in the Appendix A of the paper. Details regarding the lattice unit-cell topologies are discussed in the Supplementary Material of the paper. The results obtained are reported in Figures 4–6. The relative density was limited to the range $\bar{\rho}_L \in [0, 0.5]$ in order to limit the microscopic lattice element maximum aspect ratio, due to the assumption of *Euler-Bernoulli* beams as the constitutive model for the formulation derived in the previous section [56].

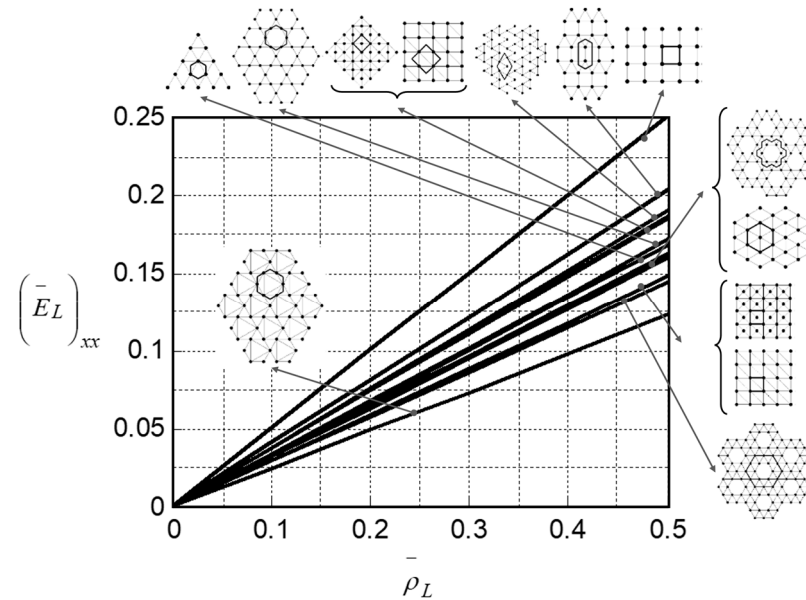


Figure 4. Relative Young’s modulus for the x -direction with respect to the relative density of the 2D LMs analyzed in the study.

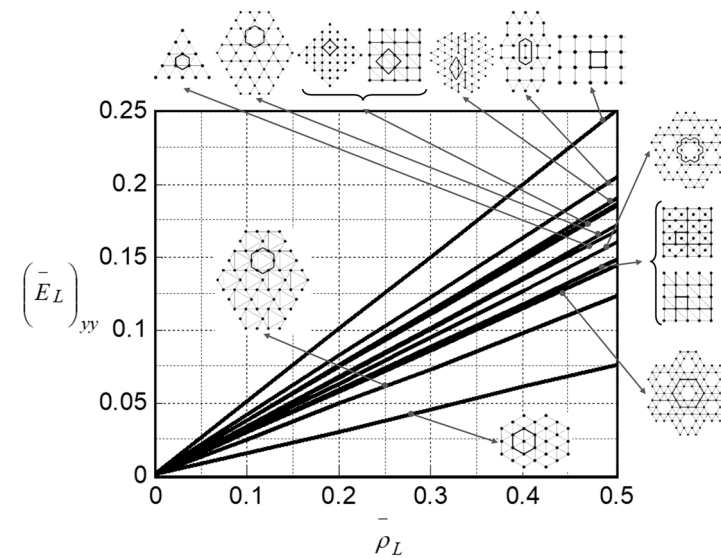


Figure 5. Relative Young’s modulus for the y -direction with respect to the relative density of the 2D LMs analyzed in the study.

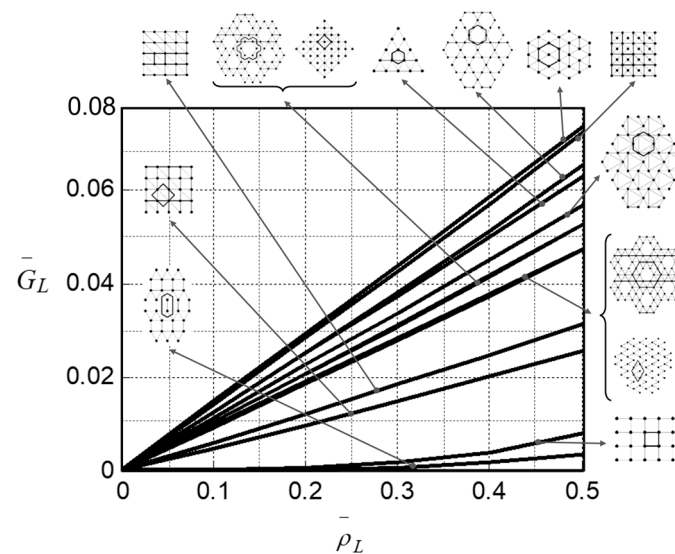


Figure 6. Relative shear modulus for the xy -direction versus relative density of the 2D LMs analyzed in the study.

Figures 4–6, the relative Young and Shear modulus of the LM with respect to a variation of relative density, the relative elastic modulus being the ratio of the LM to the solid material elastic modulus. The results are plotted for the full range of relative density; however, it should be noted that practical ranges of porosity have a reduced range of relative density depending on the porous media [57]. These charts assist in the selection of the best topology of a LM for a given design requirement. The results provide a thorough comparison of elastic properties between different LM topologies, demonstrating the proportional effect of filling the periodic voids of a LM with respect to the mechanical properties.

From Figures 4 and 5 it is possible to conclude that the axial stiffness dominates the macro-stiffness behavior of the LM. This is illustrated by the nearly-straight lines representing the variation of the relative elastic moduli versus the relative density of the LM. However, the contribution of the bending stiffness of the microscopic cell elements to the macroscopic shear stiffness of the LM is significant in LMs that have a bending dominated behavior, such as the square and the $3^3.4^2$ lattice topologies [27]. This is shown by the non-linear curves (Figure 6), representing the variation of the elastic shear moduli of the LMs versus its relative density.

From Figures 4 and 5 it can be concluded that the square lattice topology presents the most significant values of relative stiffness in both directions analyzed. This is expected due to the fact that this lattice presents the orientation of the micro-elements of the unit cell aligned with the macro-load applied. This characteristic allows the square lattice topology to be the best selection in applications where the macro-loads applied come from a single principal direction. On the other hand, the disadvantage lies in the fact that it presents a low Shear stiffness, as it can be seen in Figure 6. This makes it compliant to deform through this mechanism, when compared to other topologies, in the case of a combination of macro-loads applied in multiple directions.

The bending stiffness behavior contribution of the unit cell elements to the macro-stiffness of stretching dominated LMs can be assessed by the relations given below:

$$(\Delta \bar{E}_L)_{xx} = 100 \left((\bar{E}_L)_{xx} - (\bar{E}_L^{bar})_{xx} \right) / (\bar{E}_L)_{xx} [\%] \tag{45}$$

$$(\Delta \bar{E}_L)_{yy} = 100 \left((\bar{E}_L)_{yy} - (\bar{E}_L^{bar})_{yy} \right) / (\bar{E}_L)_{yy} [\%] \tag{46}$$

$$\Delta \bar{G}_L = 100 \left(\bar{G}_L - \bar{G}_L^{bar} \right) / \bar{G}_L [\%] \tag{47}$$

Equations (45)–(47) are plotted in Figures 7–9 for all lattice topologies considered. The curves show that the closer the topology to the full triangulated lattice, the less the participation of the micro-bending stiffness to the homogenized macro-stiffness of the LM. It is found that, at relative density 0.3, the microscopic bending contribution is almost 1% in the direct stiffness of the Kagome lattice and 2.2% in the shear stiffness of the Semi-Uni-Braced square lattice. These values can theoretically increase respectively to 8% and 17% for higher relative density, e.g., 0.9. However, for higher density the lattice cells overlap and merge together; thus, the results lose physical significance.

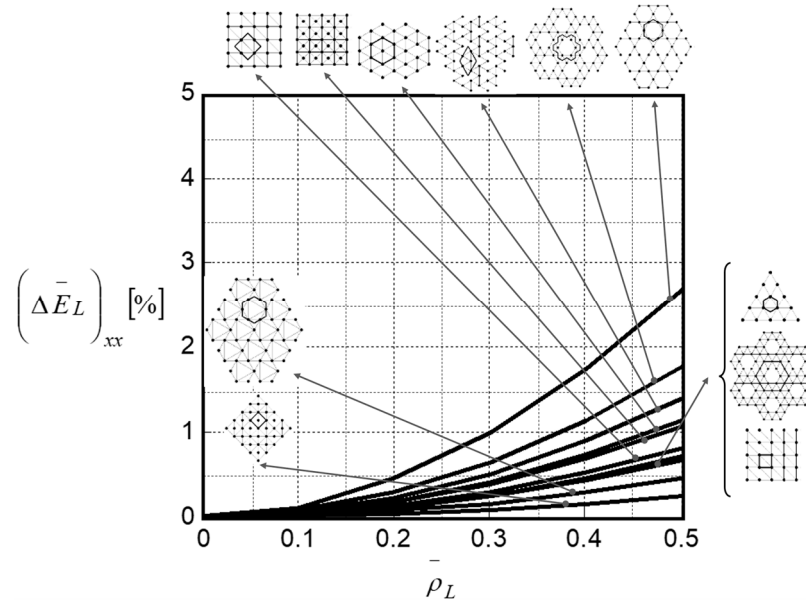


Figure 7. Contribution percentage of the bending stiffness of unit cell elements to the macroscopic Young's modulus in the x-direction versus the relative density of the LM.

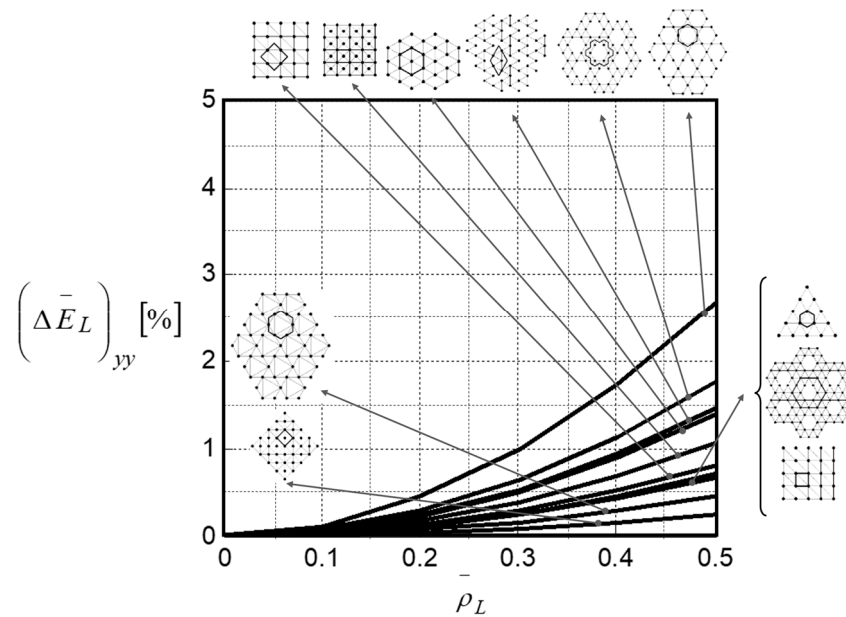


Figure 8. Contribution percentage of the bending stiffness of unit cell elements to the macroscopic Young's modulus in the y-direction versus the relative density of the LM.

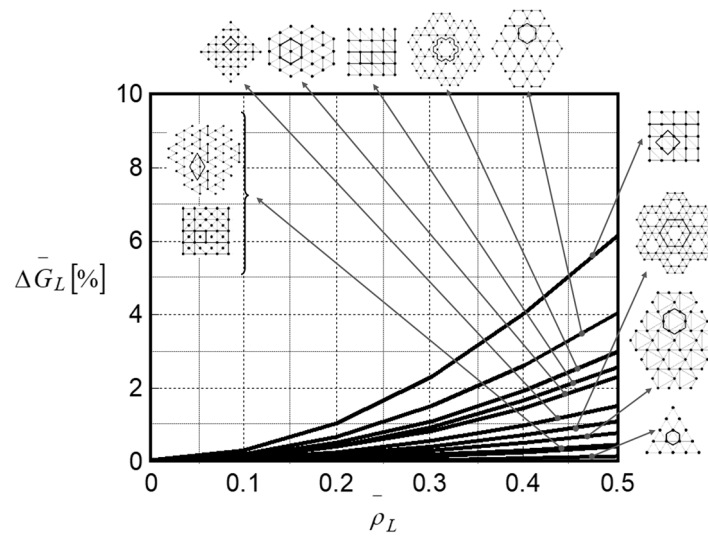


Figure 9. Contribution percentage of the bending stiffness of unit cell elements to the macroscopic shear modulus versus the relative density of the LM.

Since LMs are generally manufactured as RJLM, Figures 7–9 give an estimate of the expected error involved in the elastic properties of stretching dominated topologies that are modelled as pin-jointed lattice structures. Such analysis is useful to compare the theoretical results of pin-jointed lattices with their experimental counter parts [27]. In summary, for LMs with high relative density, the bending stiffness term in the total homogenized macroscopic stiffness increases its significance. Therefore, it becomes necessary to consider the rigid-joint modelling if one intends to achieve accurate expected results of the mechanical properties.

4. Experimental Validation

Intending to validate the theoretical model proposed, the effective elastic properties of the LM with Schafli symbol of $3^4.6$ are characterized experimentally through uniaxial tensile and pure shear quasi-static tests. The A2X Arcam Electron Beam Melting (EBM) system is utilized to manufacture the experimental specimens using the Ti6Al4V ELI Titanium Alloy. The alloy used has the mechanical properties of yield strength: $\sigma_{ys} = 940$ MPa, ultimate strength: $\sigma_{us} = 990$ MPa, Young's modulus: $E = 120$ GPa and shear modulus: $G = 45$ GPa.

4.1. Specimens Design

The LM test specimen was designed according to ElSayed and Pasini [27], in order to predict the elastic buckling and plastic yielding failure of unit cell elements, based on the solid material properties. The length of each unit cell element is set as 5 mm, such that a safety factor of 2 is adopted. To compute the tensile specimen height and width, the ASTM standards C363-00 is followed. The shear test was executed utilizing the three-rail shear method, considering the ASTM Standards, D 4255/D 4255M-01. Figure 10 depicts the dimensions utilized for the LM specimens and the test specimen installed in the three-rail shear fixture and testing machine for the shear test. Previous executed experiments demonstrated that the boundary stiffening phenomena, due to clamping of the specimen to the three-rail fixture, is minimal for dimensional ratios of specimen length with respect to unit cell size higher than 3 [58,59]. Thus, the specimen width at both sides of the testing rig is defined as 42 mm.

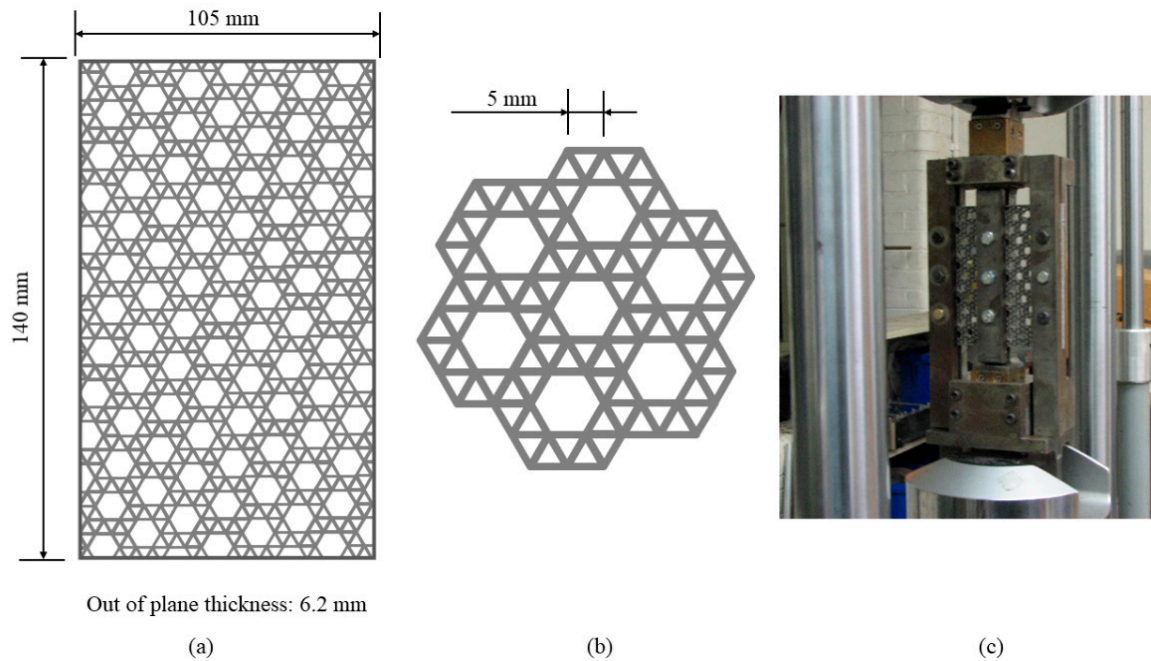


Figure 10. (a,b) Specimen LM schematics utilized in the experiment, (c) Shear LM specimen installed into the three-rail shear fixture and testing machine.

CAD models of the test specimens are created based on the designed dimensions for the different configurations. In total, six specimens are manufactured, i.e., three assigned for the different design models. Therefore, for each tensile and shear characterization, the results were based on three sets of data. The relative density of the LM is computed as 0.495 which is used to compute the stiffness and strength properties of the designed LM which are reported in Table 1.

Table 1. Comparison between the characterization results obtained with the proposed numerical model and the experimental tests.

		Numerical		Experimental	Error (%)	
		Rigid	Pin		Rigid	Pin
Tension	$(\sigma_L^y)_{xx}$ (MPa)	97.8	96.7	98.1	0.3	1.4
	E_{xxxx} (GPa)	18.8	18.6	18.9	0.5	1.5
Shear	τ_L^y (MPa)	65.1	63.0	68.7	5.5	9.04
	\bar{G} (GPa)	6.2	6.0	6.5	4.8	8.33

4.2. Experimental Set-Up and Instrumentation

The experimental set-up used is shown Figure 11. It is composed of an MTS[®] hydraulic tensile test machine with maximum applied force of 100 KN; MTS 685 hydraulic controller; 632-31E-24 extensometer; MTS FLEX Test SE data acquisition system (DAQ); a computer controlling the test using the FLEX Test SE Station Manager program (under version 3.5C 1815).



Figure 11. Experimental set-up and instrumentation. (a) 100 KN MTS machine (b) load cell (c) mounted test specimen (d) 632-31E-24 extensometer (e) DAq (f) monitoring software (g) MTS 685 hydraulic controller.

Quasi-static tests are considered employing a strain rate of magnitude of 10^{-3} s^{-1} is used [60]. The tensile test is executed until the fracture of the specimens is characterized. A ruptured tensile specimen is shown in Figure 12 and tensile test results are presented in Figure 13. Tensile yield strength is taken as the highest admissible stress achieved in the stress-strain diagram. Due the ductile nature of the material which the lattice specimens are manufactured with, the admissible stress can be estimated with a 0.2% offset of the plastic strain, parallel to the nearly straight-line elastic region of the material [61].

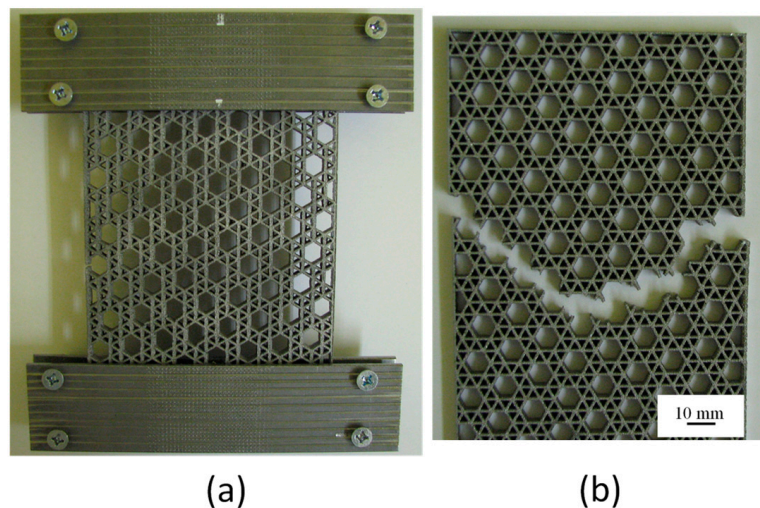


Figure 12. Tension specimens. (a) Tensile test specimen, with y -direction orientation, with the clamping device. (b) Failed LM test specimen, with x -direction orientation, tensile specimen.

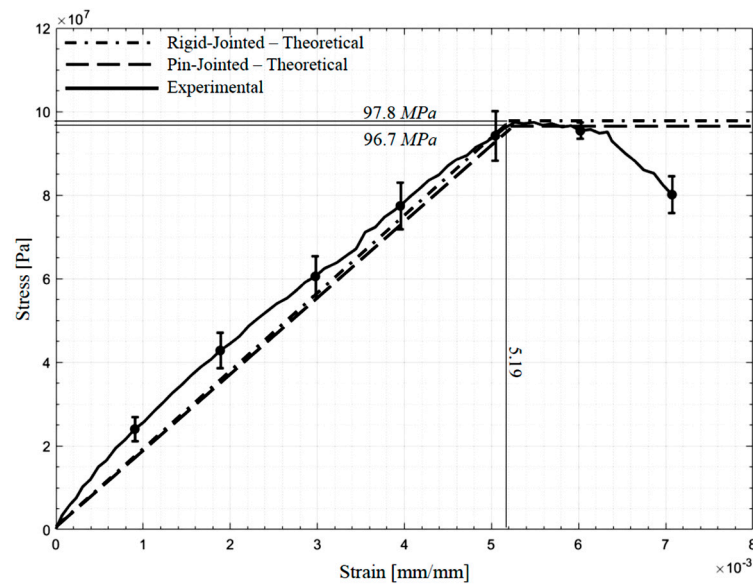


Figure 13. Results comparison of tensile test versus theoretical models.

As previously described, the standard three-rail shear method (ASTM Standards, D 4255/D 4255M-01) is utilized to execute the mechanical shear test. The load is applied at a crosshead displacement rate of 0.5 mm/min. The average shear strain rate is calculated by dividing the crosshead displacement rate by the width of the LM. This results in a rate of 1.98×10^{-4} rad/s. The test is performed until the fracture of the specimen is observed. Shear test results are shown in Figure 14. The shear yield strength is taken as the maximum stress reached during the test.

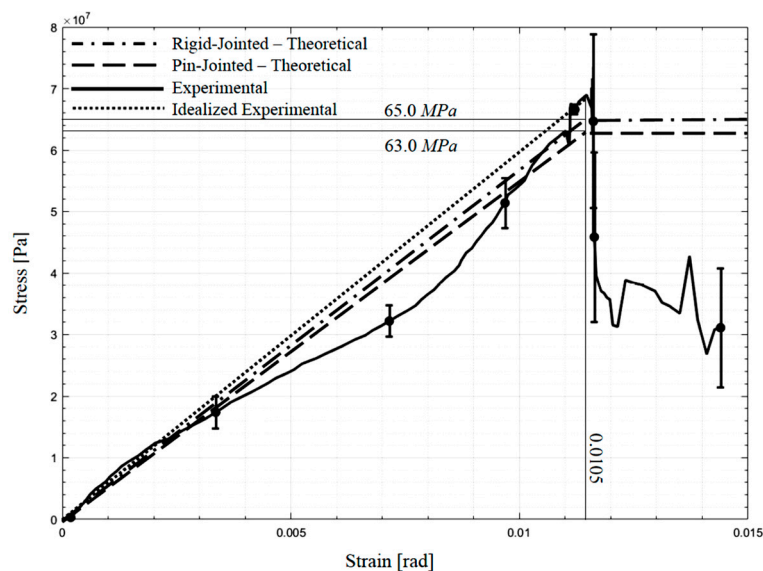


Figure 14. Results comparison of Shear test versus theoretical models.

Table 1 presents a comparison between the numerically predicted mechanical properties values and the ones experimentally obtained. The percentage error is calculated as a percentual difference between the experimental and the theoretical results. Table 1 shows that, compared to the experimental results, the model of RJLM presented in this paper can predict the homogenized mechanical properties of the LM with higher accuracy compared to those predicted by pin-jointed models. This superiority becomes significant in the shear properties prediction. This result verifies the accuracy of the theoretical model developed in this paper.

Additionally, the error propagation analysis in experimental investigations results in different origins for the source of errors for the data obtained. For instance, in the mechanical characterization of structural foams, the error propagation is significantly affected by uncertainties related to the definition of the microscopic structure of the material, because of the stochastic nature of the foam’s microstructure [62]. Another possible source of errors relies on the intrinsic hypothesis adopted for the formulation of the constitutive equations of the method. For instance, the theoretical results are obtained by considering the lattice material as a microscopic pin-jointed truss structure. This assumption implies that the axial stiffness of the microscopic cell elements is the dominant in the model. However, in reality, a LM structure is manufactured with a rigid-jointed network, and, as a consequence, the bending stiffness of the microscopic elements contributes to the overall material stiffness and strength, even if the material theoretical microstructure is kinematically determinate. Moreover, the mechanical properties of the Ti6Al4V are usually dependent upon the manufacturing technique and parameters utilized to fabricate the specimen, which affect the phase content and grain size of the solid material microstructure, thus resulting in uncertainties in the prediction of the final mechanical properties [63].

5. Anisotropic Stiffness Response of LMs

To examine the anisotropic behavior of the homogenized stiffness characteristics of LMs, consider an infinitesimal stress field, as depicted in Figure 15. The 2D stress field $(\sigma_x, \sigma_y, \tau_{xy})$ is transformed counterclockwise by an angle $\theta \in [0^\circ, 360^\circ]$ to the stress field $(\sigma_{x_\theta}, \sigma_{y_\theta}, \tau_{x_\theta y_\theta})$. To transform the material elastic properties from the $(x - y)$ coordinates to the $(x_\theta - y_\theta)$ coordinates we resort to the *Bond*-stress and strain transformation matrices [48,49,64–66]. The linearly elastic stress field in the $(x - y)$ coordinates can be related to the strain field in the same coordinate system by Hooke’s law [54]. As demonstrated by Bond [64], the stress field in the $(x - y)$ coordinates, σ , can be transformed to a stress field in the $(x_\theta - y_\theta)$ coordinates, σ_θ , using the *Bond*-Stress Transformation matrix, M_σ , such that:

$$\sigma_\theta = M_\sigma \sigma \tag{48}$$

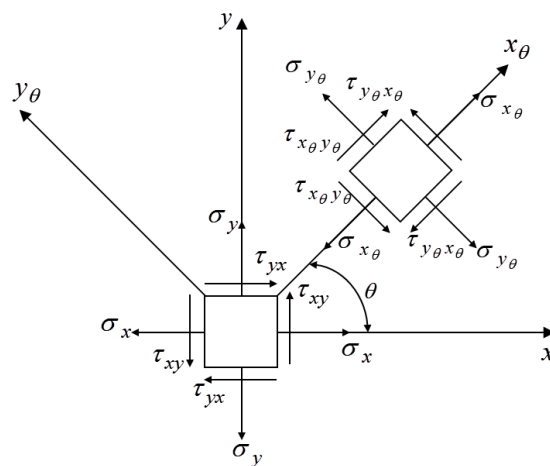


Figure 15. Infinitesimal stress field of LM.

The 2D *Bond*-Stress Transformation matrix is given by:

$$M_\sigma = \begin{bmatrix} \cos^2(\theta) & \sin^2(\theta) & \sin(2\theta) \\ \sin^2(\theta) & \cos^2(\theta) & -\sin(2\theta) \\ -0.5\sin(2\theta) & 0.5\sin(2\theta) & \cos(2\theta) \end{bmatrix} \tag{49}$$

Similarly, the corresponding strain field in the $(x - y)$ coordinates, ε , can be transformed to a strain field in the $(x_\theta - y_\theta)$ coordinates, ε_θ using the Bond-Strain Transformation matrix, M_ε , such that:

$$\varepsilon_\theta = M_\varepsilon \varepsilon \tag{50}$$

Inverting the matrices in Equations (48) and (50) and substituting the results into stress-strain relation (Hooke’s law), gives:

$$\sigma_\theta = M_\sigma K M_\varepsilon^{-1} \varepsilon_\theta \tag{51}$$

Here, $K_\theta = M_\sigma K M_\sigma^T$ where $M_\varepsilon^{-1} = M_\sigma^T$ [48]. Equation (51) is utilized to compute the transformation of the stiffness properties of LMs through an angle $\theta \in [0^\circ, 360^\circ]$. The LM relative density is set to unity, i.e., $\bar{\rho}_L = 1$. Figures 16–21 illustrate the polar diagram of the Young’s modulus (for the x_θ and y_θ directions as well as the shear modulus in the $x_\theta y_\theta$ direction) for the 13 topologies studied in this paper.

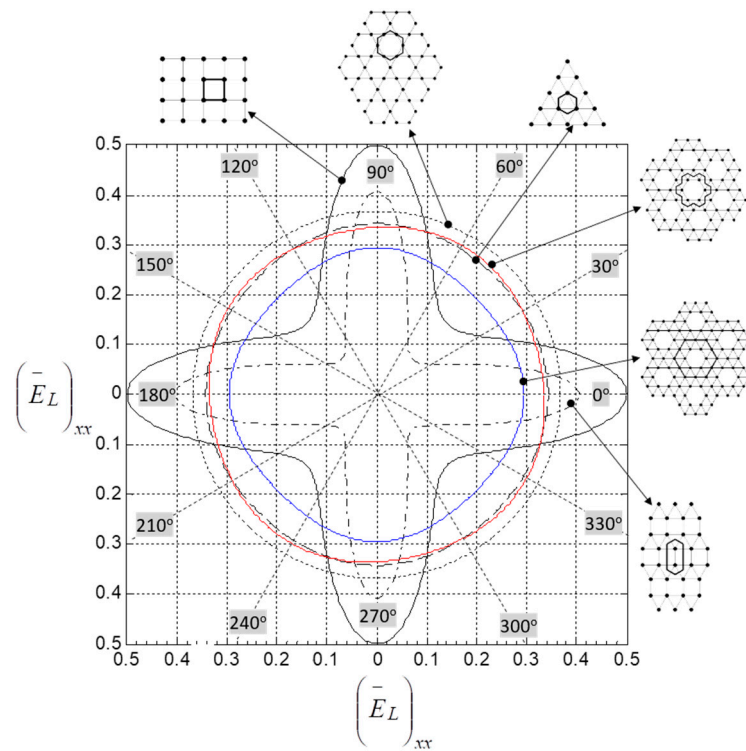


Figure 16. Polar plot showing the Young’s modulus of the LM in the x -direction as a function loading angle $\theta \in [0^\circ, 360^\circ]$.

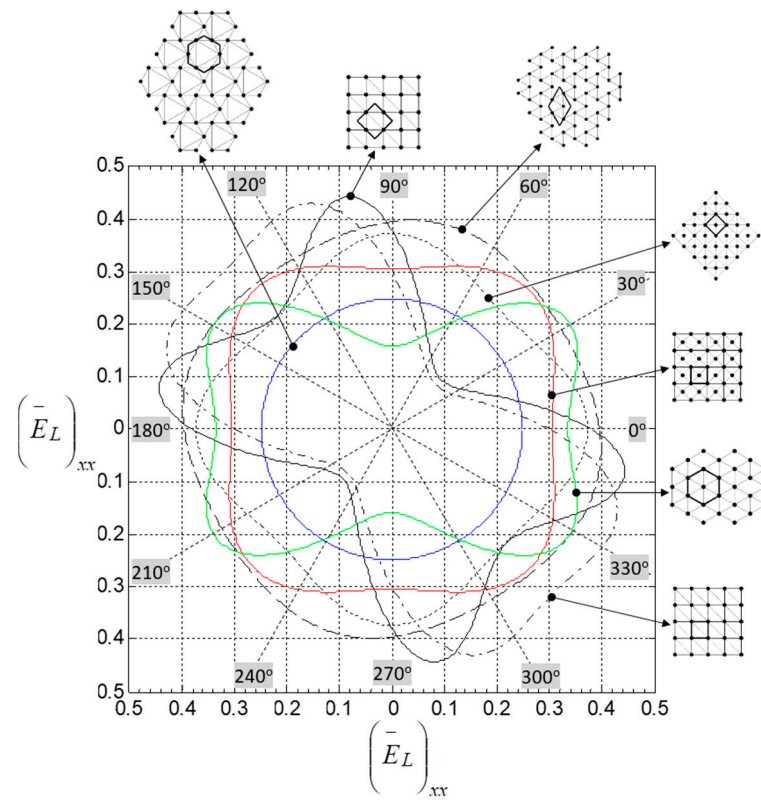


Figure 17. Polar plot showing the Young’s modulus of the LM in the x -direction as a function loading angle $\theta \in [0^\circ, 360^\circ]$.

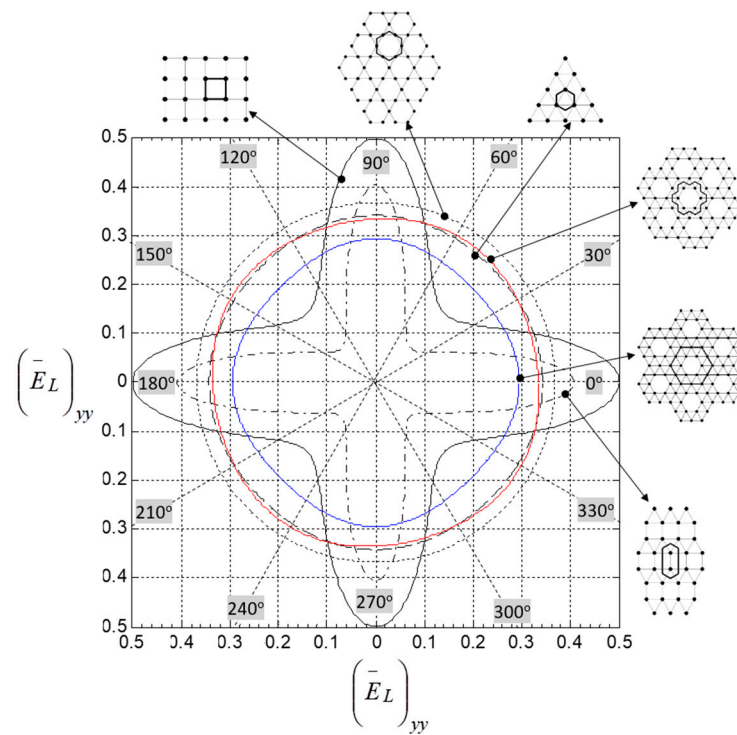


Figure 18. Polar plot showing the Young’s modulus of the LM in the y -direction as a function of loading angle $\theta \in [0^\circ, 360^\circ]$.

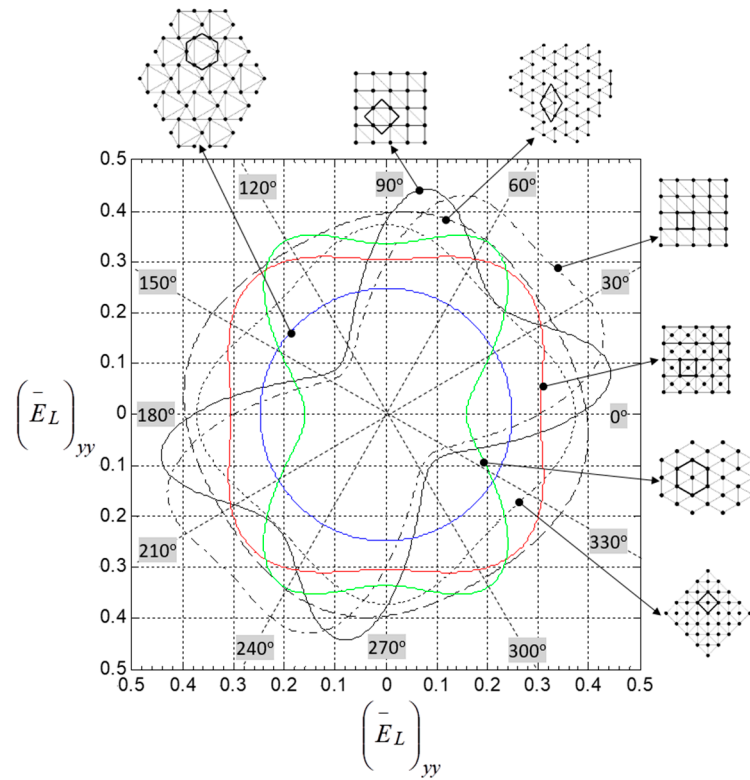


Figure 19. Polar plot showing the Young's modulus of the LM in the y -direction as a function loading angle $\theta \in [0^\circ, 360^\circ]$.

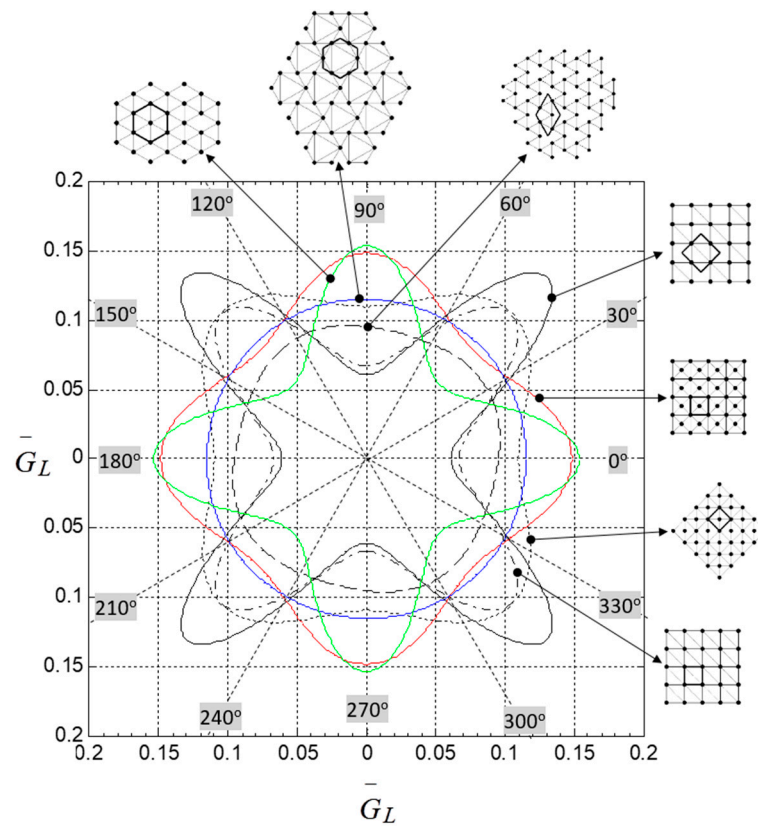


Figure 20. Polar plot showing the shear modulus of the LM as a function of loading angle $\theta \in [0^\circ, 360^\circ]$.

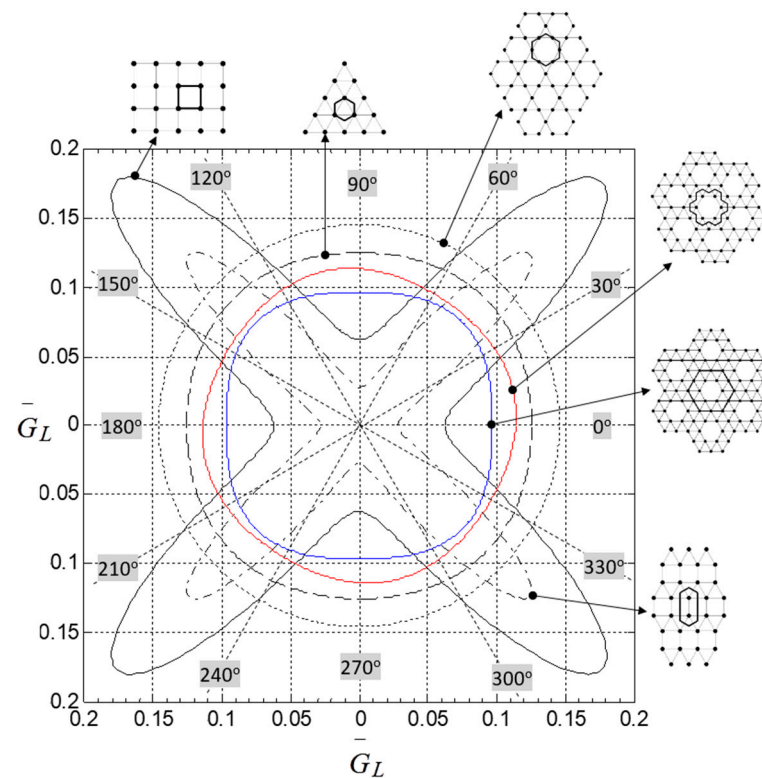


Figure 21. Polar plot showing the shear modulus of the LM as a function loading angle $\theta \in [0^\circ, 360^\circ]$.

6. Discussion and Concluding Remarks

This work presented a method to calculate the elastic properties of micro-truss LMs with rigid-jointed architecture. The procedure consists of four main steps. The first involves the use of classical matrix methods of structural analysis to determine the stiffness properties of the lattice unit cell. In the second, the Bloch's theorem is employed to generate the irreducible representation of the LM structure. The third resorts to the Cauchy-Born Hypothesis to express the microscopic nodal forces and deformations in terms of a homogenized macro-strain field applied to the lattice. Finally, the Hill-Mandel principle is used to obtain the macro-stiffness properties of the RJLM. The accuracy of the model is verified experimentally.

Using the theoretical model, three set of charts are developed, the first set, Figures 4–6, shows the variation of the elastic moduli with respect to their relative density for 13 lattice topologies. Besides cell topology, lattice orientation governs the axial stiffness of the unit cell network, which in turn influences the macroscopic stiffness of the LM. We learn from these charts the importance of examining the lattice resistant to deformation in both axial and shear direction with respect to the macroscopic loading applied to the material. For example, consider the square lattice. Its cell elements are aligned with the direction of the external loadings. Hence, the direct stiffness to mass ratio is the highest among the selected topologies. Its shear stiffness characteristics, however, are the lowest. If a macroscopic loading triggered the element shear stiffness, then its superior stiffness in the axial direction would be overshadowed by its high shear compliance. This example shows that to assess the performance of a lattice, it is necessary to consider the macroscopic load applied to the material as well as the type of deformation that this load triggers on the cell members.

The second set of charts, Figures 7–9, has been presented to estimate the errors between theoretical results of pin-jointed micro-trusses and their rigid-jointed counterpart. The charts show the participation of the bending stiffness of stretching dominated unit cell beams to the homogenized macro-stiffness. For a stretching dominated LM, the main observation is that the closer the cell topology to the full triangulation, the less the cell elements contribute to the bending stiffness. In particular, the contribution is negligible

for lattice structures that possess no microscopic internal mechanisms in their pin-jointed versions of the lattice. At 0.3 relative density, we find that the bending resistant of the Kagome lattice members contribute up to 1% to the total stiffness of the material. This is the highest contribution among the selected topologies. On the other hand, at the same relative density, the bending stiffness contribution of the cell members is limited to 0.3% for the Uni-Braced square lattice topology, which has internal mechanisms.

Finally, the third set of plots, Figures 15–20, includes polar diagrams showing the magnitude of the elastic moduli in response to a load from any in-plane direction. These charts provide insight into their anisotropic as well as indicate the best orientation a LM can be loaded to withstand a macroscopic loading applied in a given direction. For instance, the fully triangulated lattice is isotropic. Its properties represented by a circle are invariant to the direction of the macroscopic loading. The square lattice, on the other hand, has orthotropic characteristics, as illustrated by the four-point star shape of the moduli. The DHT and $3^4.6$ topologies exhibit quasi-isotropic stiffness properties as shown by the roughly circular plot of the variation of their elastic moduli correspondent to the direction of macroscopic loading.

The three set of charts depicted in this paper can be used for analysis and design purposes of LM. In general, the charts might help to gain insight into the selection of the best lattice topology for a given design application, as well as to explore the potential of novel lattice topologies in populating unfilled areas of the material properties charts.

Supplementary Materials: The supporting information for the paper is available online at <https://www.mdpi.com/article/10.3390/applmech2020020/s1>.

Author Contributions: V.E.L.G. and M.S.A.E. conceived this paper. V.E.L.G. and M.S.A.E. drafted the original manuscript. Both authors have read and agreed to the published version of the manuscript.

Funding: This research received no external funding.

Informed Consent Statement: Not applicable.

Data Availability Statement: The data presented in this study are available on request from the corresponding author.

Acknowledgments: The authors acknowledge the financial support provided by The Natural Sciences and Engineering research Council of Canada (NSERC).

Conflicts of Interest: The authors declare no conflict of interest.

Appendix A

The nomenclature of the lattice topologies investigated in this paper are summarized in the Figure A1.

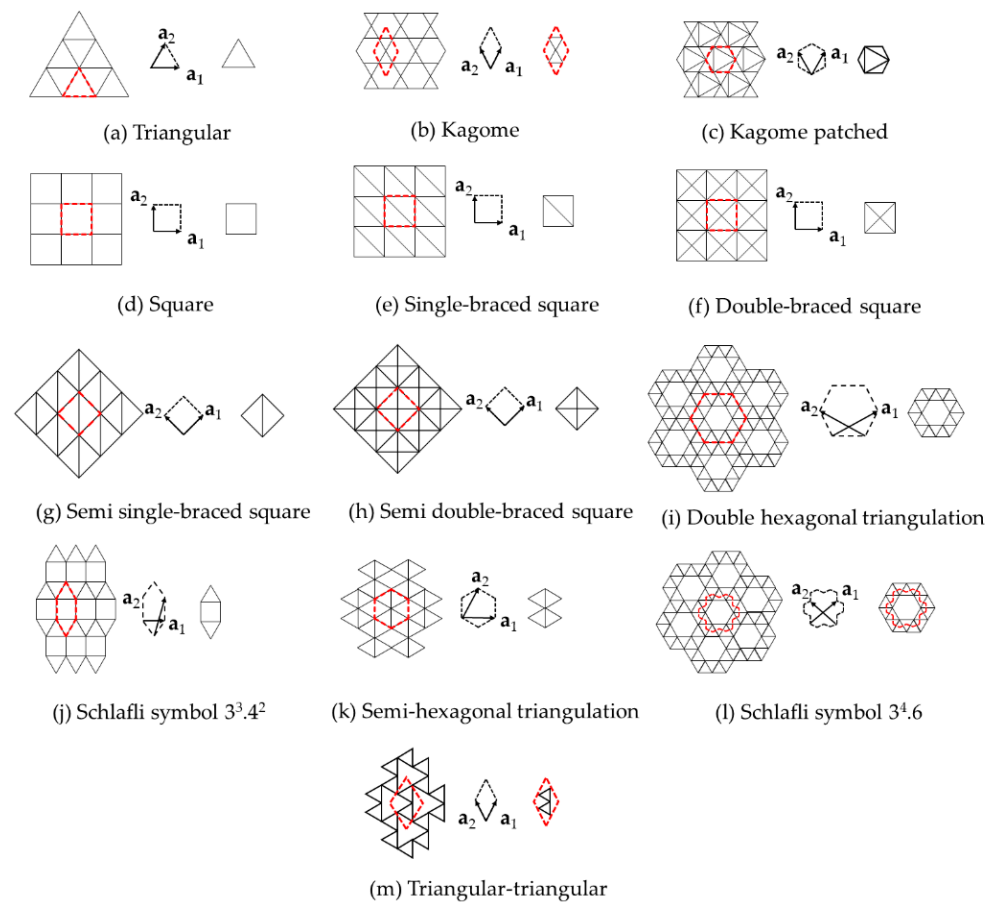


Figure A1. Lattice topologies investigated in the study. Unit-cells: (a) Triangular, (b) Kagome, (c) Kagome patched, (d) Square, (e) Single-braced square, (f) Double-braced square, (g) Semi single-braced square, (h) Semi double-braced square, (i) Double hexagonal triangulation, (j) Schläfli symbol $3^3.4^2$, (k) Semi-hexagonal triangulation, (l) Schläfli symbol $3^4.6$, (m) Triangular-triangular.

References

- Hill, R. Elastic properties of reinforced solids: Some theoretical principles. *J. Mech. Phys. Solids* **1963**, *11*, 357–372. [[CrossRef](#)]
- Shan, Z.; Gokhale, A.M. Representative volume element for non-uniform micro-structure. *Comput. Mater. Sci.* **2002**, *24*, 361–379. [[CrossRef](#)]
- Drugan, W.J.; Willis, J.R. A micromechanics-based nonlocal constitutive equation and estimates of representative volume element size for elastic composites. *J. Mech. Phys. Solids* **1996**, *44*, 497–524. [[CrossRef](#)]
- Brillouin, L. *Wave Propagation in Periodic Structures: Electric Filters and Crystal Lattices*; Dover phoenix editions; Dover Publications: Mineola, NY, USA, 2003; ISBN 9780486495569.
- Chen, Y.; Li, T.; Scarpa, F.; Wang, L. Lattice Metamaterials with Mechanically Tunable Poisson's Ratio for Vibration Control. *Phys. Rev. Appl.* **2017**, *7*. [[CrossRef](#)]
- D'Alessandro, L.; Zega, V.; Ardito, R.; Corigliano, A. 3D auxetic single material periodic structure with ultra-wide tunable bandgap. *Sci. Rep.* **2018**, *8*, 1–9. [[CrossRef](#)]
- Arretche, I.; Matlack, K.H. Experimental Testing of Vibration Mitigation in 3D-Printed Architected Metastructures. *J. Appl. Mech.* **2019**, *86*, 1–10. [[CrossRef](#)]
- Totaro, G.; Gürdal, Z. Optimal design of composite lattice shell structures for aerospace applications. *Aerosp. Sci. Technol.* **2009**, *13*, 157–164. [[CrossRef](#)]
- Nasrullah, A.I.H.; Santosa, S.P.; Dirgantara, T. Design and optimization of crashworthy components based on lattice structure configuration. *Structures* **2020**, *26*, 969–981. [[CrossRef](#)]
- Vasiliev, V.V.; Razin, A.F. Anisogrid composite lattice structures for spacecraft and aircraft applications. *Compos. Struct.* **2006**, *76*, 182–189. [[CrossRef](#)]
- Martorelli, M.; Gloria, A.; Bignardi, C.; Cali, M.; Maietta, S. Design of Additively Manufactured Lattice Structures for Biomedical Applications. *J. Healthc. Eng.* **2020**, *2020*, 2707560. [[CrossRef](#)]

12. Abate, K.M.; Nazir, A.; Yeh, Y.-P.; Chen, J.-E.; Jeng, J.-Y. Design, optimization, and validation of mechanical properties of different cellular structures for biomedical application. *Int. J. Adv. Manuf. Technol.* **2020**, *106*, 1253–1265. [[CrossRef](#)]
13. Seharing, A.; Azman, A.H.; Abdullah, S. Finite element analysis of gradient lattice structure patterns for bone implant design. *Int. J. Struct. Integr.* **2020**, *11*, 535–545. [[CrossRef](#)]
14. Tan, X.; Chen, S.; Wang, B.; Tang, J.; Wang, L.; Zhu, S.; Yao, K.; Xu, P. Real-time tunable negative stiffness mechanical metamaterial. *Extrem. Mech. Lett.* **2020**, *41*, 100990. [[CrossRef](#)]
15. Liu, K.; Han, L.; Hu, W.; Ji, L.; Tao, R.; Wan, Z.; Yang, X.; Wei, Y.; Dai, Z.; Zhao, Z.; et al. 4D printed zero Poisson's ratio metamaterial with switching function of mechanical and vibration isolation performance. *Mater. Des.* **2020**, 109153. [[CrossRef](#)]
16. Zhang, K.; Zhao, P.; Zhao, C.; Hong, F.; Deng, Z. Study on the mechanism of band gap and directional wave propagation of the auxetic chiral lattices. *Compos. Struct.* **2020**, *238*, 111952. [[CrossRef](#)]
17. Schaedler, T.A.; Jacobsen, A.J.; Torrents, A.; Sorensen, A.E.; Lian, J.; Greer, J.R.; Valdevit, L.; Carter, W.B. Ultralight Metallic Microlattices. *Science* **2011**, *334*, 962–965. [[CrossRef](#)]
18. El-Sayed, M.A.; Essa, K.; Ghazy, M.; Hassanin, H. Design optimization of additively manufactured titanium lattice structures for biomedical implants. *Int. J. Adv. Manuf. Technol.* **2020**, *110*, 2257–2268. [[CrossRef](#)]
19. Zheng, X.; Lee, H.; Weisgraber, T.H.; Shusteff, M.; DeOtte, J.; Duoss, E.B.; Kuntz, J.D.; Biener, M.M.; Ge, Q.; Jackson, J.A.; et al. Ultralight, ultrastiff mechanical metamaterials. *Science* **2014**, *344*, 1373–1377. [[CrossRef](#)]
20. Muhammad; Lim, C.W.; Li, J.T.H.; Zhao, Z. Lightweight architected lattice phononic crystals with broadband and multiband vibration mitigation characteristics. *Extrem. Mech. Lett.* **2020**, *41*, 100994. [[CrossRef](#)]
21. Zhao, P.; Zhang, K.; Deng, Z. Elastic Wave Propagation in Lattice Metamaterials with Koch Fractal. *Acta Mech. Solida Sin.* **2020**, *33*, 600–611. [[CrossRef](#)]
22. Tancogne-Dejean, T.; Spierings, A.B.; Mohr, D. Additively-manufactured metallic micro-lattice materials for high specific energy absorption under static and dynamic loading. *Acta Mater.* **2016**, *116*, 14–28. [[CrossRef](#)]
23. Chen, X.; Ji, Q.; Wei, J.; Tan, H.; Yu, J.; Zhang, P.; Laude, V.; Kadic, M. Light-weight shell-lattice metamaterials for mechanical shock absorption. *Int. J. Mech. Sci.* **2020**, *169*, 105288. [[CrossRef](#)]
24. Yang, C.; Li, Q.M. Advanced lattice material with high energy absorption based on topology optimisation. *Mech. Mater.* **2020**, *148*. [[CrossRef](#)]
25. Deshpande, V.S.; Ashby, M.F.; Fleck, N.A. Foam topology: Bending versus stretching dominated architectures. *Acta Mater.* **2001**, *49*, 1035–1040. [[CrossRef](#)]
26. Evans, A.G.; Hutchinson, J.W.; Fleck, N.A.; Ashby, M.F.; Wadley, H.N.G. The topological design of multifunctional cellular metals. *Prog. Mater. Sci.* **2001**, *46*, 309–327. [[CrossRef](#)]
27. Elsayed, M.S.A.; Pasini, D. Analysis of the elastostatic specific stiffness of 2D stretching-dominated lattice materials. *Mech. Mater.* **2010**, *42*, 709–725. [[CrossRef](#)]
28. Elsayed, M.S.A.; Pasini, D. Multiscale structural design of columns made of regular octet-truss lattice material. *Int. J. Solids Struct.* **2010**, *47*, 1764–1774. [[CrossRef](#)]
29. Wang, A.J.; McDowell, D.L. In-plane stiffness and yield strength of periodic metal honeycombs. *J. Eng. Mater. Technol. Trans. ASME* **2004**, *126*, 137–156. [[CrossRef](#)]
30. Cho, Y.; Shin, J.-H.; Costa, A.; Kim, T.A.; Kunin, V.; Li, J.; Lee, S.Y.; Yang, S.; Han, H.N.; Choi, I.-S.; et al. Engineering the shape and structure of materials by fractal cut. *Proc. Natl. Acad. Sci. USA* **2014**, *111*, 17390–17395. [[CrossRef](#)]
31. Alkhader, M.; Nazzal, M.; Louca, K. Design of bending dominated lattice architectures with improved stiffness using hierarchy. *Proc. Inst. Mech. Eng. Part C J. Mech. Eng. Sci.* **2019**, *233*, 3976–3993. [[CrossRef](#)]
32. Timoshenko, S.P.; Gere, J.M. *Theory of Elastic Stability*; Dover Civil and Mechanical Engineering; Dover Publications: Mineola, NY, USA, 2012; ISBN 9780486134802.
33. Noor, A.K.; Nemeth, M.P. Micropolar beam models for lattice grids with rigid joints. *Comput. Methods Appl. Mech. Eng.* **1980**, *21*, 249–263. [[CrossRef](#)]
34. Bažant, Z.P.; Christensen, M. Analogy between micropolar continuum and grid frameworks under initial stress. *Int. J. Solids Struct.* **1972**, *8*, 327–346. [[CrossRef](#)]
35. ERINGEN, A.C. Theory of Micropolar Fluids. *J. Math. Mech.* **1966**, *16*, 1–18. [[CrossRef](#)]
36. Bloch, F. Über die Quantenmechanik der Elektronen in Kristallgittern. *Z. Phys.* **1929**, *52*, 555–600. [[CrossRef](#)]
37. Hutchinson, R. Mechanics of Lattice Materials. Ph.D. Thesis, University of Cambridge, Cambridge, UK, 2005.
38. Hutchinson, R.G.; Fleck, N.A. The structural performance of the periodic truss. *J. Mech. Phys. Solids* **2006**, *54*, 756–782. [[CrossRef](#)]
39. Gasparetto, V.E.L.; ElSayed, M.S.A. Multiscale Optimization of Specific Elastic Properties and Microscopic Frequency Band-gaps of Architected Microtruss Lattice Materials. *Int. J. Mech. Sci.* **2021**, *197*, 106320. [[CrossRef](#)]
40. Gasparetto, V.E.L.; ElSayed, M.S.A. Shape transformers for phononic band gaps tuning in two-dimensional Bloch-periodic lattice structures. *Eur. J. Mech. A/Solids* **2021**, *89*, 104278. [[CrossRef](#)]
41. Niu, B.; Wang, B. Directional mechanical properties and wave propagation directionality of Kagome honeycomb structures. *Eur. J. Mech. A/Solids* **2016**, *57*, 45–58. [[CrossRef](#)]
42. McCormac, J.C. *Structural Analysis: Using Classical and Matrix Methods*; John Wiley & Sons: Hoboken, NJ, USA, 2006; ISBN 9780470036082.

43. Bhattacharya, K. *Microstructure of Martensite: Why It Forms and How It Gives Rise to the Shape-Memory Effect*; Oxford Series on Materials Modelling; Oxford University Press: Oxford, UK, 2003; ISBN 9780198509349.
44. Born, M.; Huang, K. *Dynamical Theory of Crystal Lattices*; International Series of Monographs on Physics; Clarendon Press: Oxford, UK, 1988; ISBN 9780198503699.
45. Maugin, G.A.; Crighton, D.G. *The Thermomechanics of Plasticity and Fracture*; Cambridge Texts in Applied Mathematics; Cambridge University Press: Cambridge, UK, 1992; ISBN 9780521397803.
46. Pitteri, M.A.; Zanzotto, G.A.; Rossit, C.A.R. Continuum Models for Phase Transitions and Twinning in Crystals. *Applied Mathematics*, Volume 19. *Appl. Mech. Rev.* **2003**, *56*, B59. [[CrossRef](#)]
47. Timoshenko, S.; Young, D.H. *Theory of Structures*; McGraw-Hill Book Company: New York, NY, USA, 1945.
48. Auld, B.A. *Acoustic Fields and Waves in Solids*; A Wiley-Interscience publication; John Wiley & Sons: Hoboken, NJ, USA, 1973; ISBN 9785885013437.
49. Hoffmeister, B.K.; Smith, S.R.; Handley, S.M.; Rho, J.Y. Anisotropy of Young's modulus of human tibial cortical bone. *Med. Biol. Eng. Comput.* **2000**, *38*, 333–338. [[CrossRef](#)]
50. Grosso, G.; Parravicini, G.P. *Solid State Physics*; Elsevier Science: Amsterdam, The Netherlands, 2000; ISBN 9780123044600.
51. Jones, W.; March, N.H. *Theoretical Solid State Physics*; Dover Books on Physics and Chemistry; Dover Publications: Mineola, NY, USA, 1985; ISBN 9780486650166.
52. Langley, R.S. A Note On The Force Boundary Conditions For Two-Dimensional Periodic Structures With Corner Freedoms. *J. Sound Vib.* **1993**, *167*, 377–381. [[CrossRef](#)]
53. Langley, R.S.; Bardell, N.S.; Ruivo, H.M. The response of two-dimensional periodic structures to harmonic point loading: A theoretical and experimental study of a beam grillage. *J. Sound Vib.* **1997**, *207*, 521–535. [[CrossRef](#)]
54. Renton, J.D. *Elastic Beams and Frames*; Woodhead Publishing Series in Civil and Structural Engineering; Elsevier Science: Amsterdam, The Netherlands, 2002; ISBN 9780857099624.
55. Strang, G. *Introduction to Linear Algebra*; Wellesley-Cambridge Press: Wellesley, MA, USA, 1993; ISBN 9780961408800.
56. Petyt, M. *Introduction to Finite Element Vibration Analysis*; Cambridge University Press: Cambridge, UK, 1998; ISBN 9780521634175.
57. Kováčik, J. Correlation between Young's modulus and porosity in porous materials. *J. Mater. Sci. Lett.* **1999**, *18*, 1007–1010. [[CrossRef](#)]
58. Gibson, L.J.; Ashby, M.F. *Cellular Solids: Structure and Properties*; Cambridge Solid State Science Series; Cambridge University Press: Cambridge, UK, 1999; ISBN 9780521499118.
59. Ashby, M.F.; Evans, T.; Ashby, M.F.; Evans, A.G.; Fleck, N.A.; Gibson, L.J.; Hutchinson, J.W.; Wadley, H.N.G. *Metal Foams: A Design Guide*; Butterworth-Heinemann: Amsterdam, The Netherlands, 2000; ISBN 9780750672191.
60. Lee, S.; Barthelat, F.; Moldovan, N.; Espinosa, H.D.; Wadley, H.N.G. Deformation rate effects on failure modes of open-cell Al foams and textile cellular materials. *Int. J. Solids Struct.* **2006**, *43*, 53–73. [[CrossRef](#)]
61. Cahoon, J.R.; Broughton, W.H.; Kutzak, A.R. The determination of yield strength from hardness measurements. *Metall. Trans.* **1971**, *2*, 1979–1983. [[CrossRef](#)]
62. Ramamurty, U.; Paul, A. Variability in mechanical properties of a metal foam. *Acta Mater.* **2004**, *52*, 869–876. [[CrossRef](#)]
63. Engel, B.; Bourell, D.L. Titanium alloy powder preparation for selective laser sintering. *Rapid Prototyp. J.* **2000**, *6*, 97–106. [[CrossRef](#)]
64. Bond, W.L. The Mathematics of the Physical Properties of Crystals. *Bell Syst. Tech. J.* **1943**, *22*, 1–72. [[CrossRef](#)]
65. Hearmon, R.F.S. The Elastic Constants of Anisotropic Materials. *Rev. Mod. Phys.* **1946**, *18*, 409–440. [[CrossRef](#)]
66. Lin, B.; Giurgiutiu, V. Power and energy transduction analysis of piezoelectric wafer-active sensors for structural health monitoring. *Struct. Health Monit.* **2012**, *11*, 109–121. [[CrossRef](#)]